4-2014

Rigorous Investigation of the Array-tilt Aberration for Hexagonal, Optical Phased Arrays

Milo W. Hyde IV

Jason E. Wyman

Glenn A. Tyler

Rigorous investigation of the array-tilt aberration for hexagonal, optical phased arrays

Milo W. Hyde IV,[1,*] Jason E. Wyman,[1] and Glenn A. Tyler[2]

[1]Air Force Institute of Technology, 2950 Hobson Way, Dayton, Ohio 45433, USA

[2]The Optical Sciences Company, 1341 South Sunkist Street, Anaheim, California 92806-5614, USA

*Corresponding author: milo.hyde@afit.edu

Received 17 January 2014; accepted 24 February 2014;
posted 26 February 2014 (Doc. ID 204939); published 7 April 2014

An investigation of the array-tilt aberration for hexagonal, optical phased arrays is presented. The investigation begins with theoretical derivations of the far-zone radiated field, the array factor, and the far-field radiated power for the seven-element hexagonal array with array tilt present. Physical insights gained from this analysis are discussed. An analytical treatment of correlation-based array-tilt estimators is also undertaken. Two novel array-tilt estimation techniques are developed from the analysis. The new techniques are shown to be significantly more efficient computationally than the traditional estimation approach. Simulation and experimental results are presented to validate the new array-tilt estimation methods.

OCIS codes: (140.3290) Laser arrays; (140.3298) Laser beam combining; (140.3510) Lasers, fiber; (230.6120) Spatial light modulators.

http://dx.doi.org/10.1364/AO.53.002416

1. Introduction

Recent laser weapons research has focused on reducing the size and weight requirements of the system to make laser weapons more applicable. Traditional monolithic laser weapon systems, e.g., the US Air Force Airborne Laser [1–3], employ chemical lasers to produce the high power outputs required for weapon effectiveness. The size and weight of the laser systems makes employing a monolithic design infeasible for all but the largest aircraft [1,2].

Fiber lasers offer a solution to the size and weight problem, providing a compact, reliable, and rugged laser source [4–6]. However, physical limitations from nonlinear effects and optical damage have hindered development of fiber lasers to the power ranges required for laser weapons [7]. While it is currently unfeasible to construct a monolithic fiber laser weapon, high power outputs can be achieved by combining the beams of multiple fiber lasers arranged in an array.

There are two beam combining techniques—incoherent and coherent. Systems that utilize incoherent beam combining, like the US Navy Laser Weapon [8], can approach a maximum peak target irradiance that is N (where N is the number of array elements) times that produced by a single array element [5,6,8]. For systems employing coherent beam combining, peak target irradiance scales by N^2 times that of a single array element [4–6], thus, making coherent beam combining a more suitable approach for smaller platforms, such as small aircraft.

Coherent beam combining has been utilized by the RF/microwave community for over a century [9]. Because of the much shorter wavelength (much higher frequency), element phasing at optical wavelengths is much more difficult to achieve due to the need to detect phase differences between elements to well within a wavelength, as well as the needs for polarization control and narrow-linewidth fiber lasers [4–7]. Despite these challenges, coherent beam combining at optical wavelengths has been achieved using techniques such as locking of optical coherence by single-detector electronic-frequency tagging (LOCSET), which produces a 1.4 kW laser beam

by combining 16 narrow-linewidth 100 W fiber lasers [6,10,11].

Techniques such as LOCSET, phase the laser elements before light leaves the system and, therefore, do not account or correct for aberrations encountered in propagation from the source to the target, i.e., aberrations due to atmospheric turbulence, aero-optical effects, the target, etc. [7]. Recent work by Tyler [12] has shown that it is possible to estimate and separate the telescopic, atmospheric, and target (speckle) aberrations, thus making the concept of a laser array, which phases on target, a possibility. In his work, Tyler showed that several low-order (and relatively benign) aberrations were unobservable [12]. One of these modes is termed array tilt (the focus of this work) and can be visualized as a discrete (stair-step) phase ramp across the array. Array tilt is undesired because it has the effect of transferring power from the main array lobe into the grating lobes thereby decreasing power in the bucket and reducing the effectiveness of the weapon. Note that since array tilt is unobservable, it must be measured or estimated using a separate system—typically an imager combined with a correlation-based estimator [13].

This paper undertakes a rigorous investigation of the array-tilt aberration in order to develop more efficient techniques to estimate and ultimately correct for array tilt. A theoretical investigation of array tilt is presented in Section 2. In this section, the far-zone radiated field, array factor (AF), and far-field radiated power, are derived and discussed for the seven-element regular hexagonal array—a common array shape because it maximizes the number of circular elements while minimizing the overall array area (Thue's theorem on circle packing). A theoretical investigation of correlation-based array-tilt estimators is also included. From the insights gained via this analysis, two novel array-tilt estimation techniques are presented and discussed. In Section 3, the two new estimation techniques are validated using simulations and experiments. Lastly, this paper is concluded with brief summaries of the presented work and significant contributions.

2. Methodology

Consider the seven-element hexagonal array depicted in Fig. 1. The identical array elements, represented here as circles, have diameters d. The elements are arranged in a regular hexagon with D center-to-center adjacent element spacings. For convenience, the x' and y' element center locations are provided in the figure. It should be noted that d, $D \gg \lambda$ (typically 10^3–$10^4\lambda$), and thus mutual coupling effects, can be safely neglected.

In accordance with classic array theory, the far-zone radiated electric field is the single element far-zone field times the AF [14], viz.

$$\boldsymbol{E}^{\mathrm{rad}}(\boldsymbol{r}) \approx jk\frac{e^{-jkr}}{r}\boldsymbol{e}^{\mathrm{rad}}\left[\left(\frac{d}{2}\right)^2\frac{J_1\left(k\frac{d}{2}\sin\theta\right)}{k\frac{d}{2}\sin\theta}\right]\mathrm{AF}(\theta,\phi), \quad (1)$$

where $k = 2\pi/\lambda$, r is the Euclidean distance from the source plane (x'-y' plane) origin to the observation point, θ and ϕ are the observation spherical angles, and J_1 is a first-order Bessel function of the first kind. The last remaining undefined symbol in Eq. (1) is the polarization factor $\boldsymbol{e}^{\mathrm{rad}} = (\hat{\phi}\,\hat{\theta} - \hat{\theta}\,\hat{\phi}) \cdot (\boldsymbol{e}^{\mathrm{inc}} \times \hat{z})$, where $\boldsymbol{e}^{\mathrm{inc}}$ is the polarization vector of the incident electric field.

In Eq. (1), it has been assumed that the magnitude and phase of the incident field is constant over each individual array element, i.e., $\boldsymbol{E}^{\mathrm{inc}}$ is not a function of x' and y'. Note that this does not preclude each element from being individually phased; element phasing is included in the AF discussed below. Last, for paraxial observation, $\sin\theta \approx \theta \approx \rho/z$, $\hat{\boldsymbol{r}} \cdot \hat{\boldsymbol{x}} \approx x/z$, and $\hat{\boldsymbol{r}} \cdot \hat{\boldsymbol{y}} \approx y/z$.

A. Seven-Element Hexagonal AF

Since array tilt is an undesired manifestation of a phase ramp across the array, the term of interest in Eq. (1) is the AF. In this section, a general expression for the seven-element hexagonal AF is derived and discussed.

The AF for the array depicted in Fig. 1 can be derived by replacing the elements with point sources located at the center of each element. Applying the principle of superposition, the AF becomes

$$\mathrm{AF} = \sum_{i=1}^{7} e^{j\varphi_i}\int_{-\infty}^{\infty}\delta(\boldsymbol{r}_i - \boldsymbol{r}')e^{jk\hat{\boldsymbol{r}}\cdot\boldsymbol{r}'}\mathrm{d}^3r' = \sum_{i=1}^{7} e^{j\varphi_i}e^{jk\hat{\boldsymbol{r}}\cdot\boldsymbol{r}_i}, \quad (2)$$

where φ_i represents the phase commanded to element i, $\boldsymbol{r}' = \hat{\boldsymbol{x}}x' + \hat{\boldsymbol{y}}y' + \hat{z}z'$, and $\boldsymbol{r}_i = \hat{\boldsymbol{x}}x_i + \hat{\boldsymbol{y}}y_i + \hat{z}0$ is a vector that points from the source plane origin to the center of element i.

When array tilt is present, φ_i takes the form of a discretized plane, i.e.,

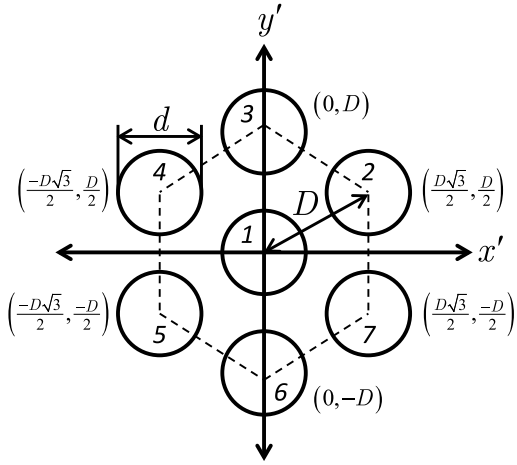

Fig. 1. Schematic of a seven-element hexagonal array composed of identical circular elements. The diameter of each element is d; the spacing between adjacent elements is D. For the reader's convenience, the (x', y') element center coordinates are annotated on the figure.

$$\varphi_i = \frac{2\varphi_x}{D\sqrt{3}}x_i + \frac{2\varphi_y}{D}y_i, \tag{3}$$

where φ_x and φ_y are the amounts of array tilt in radians in the x and y directions, respectively. Note that array tilt is commonly expressed in waves, thus $\varphi_x = 2\pi W_x$ and $\varphi_y = 2\pi W_y$.

Substituting Eq. (3) into Eq. (2), inserting the element center locations (x_i, y_i), and simplifying yields

$$\mathrm{AF} = \sum_{m=-2}^{2}\sum_{n=-1}^{1} a_{mn}\left(e^{j2\pi W_y m}e^{jk\hat{\mathbf{r}}\cdot\hat{\mathbf{y}}\frac{D}{2}m}\right)\left(e^{j2\pi W_x n}e^{jk\hat{\mathbf{r}}\cdot\hat{\mathbf{x}}\frac{D\sqrt{3}}{2}n}\right), \tag{4}$$

where $a_{mn} = \eta_{1m}\xi_{1n} + \eta_{2m}\xi_{2n}$. Here, $\boldsymbol{\eta}_1$, $\boldsymbol{\xi}_1$, $\boldsymbol{\eta}_2$, and $\boldsymbol{\xi}_2$ are

$$\begin{aligned} \boldsymbol{\eta}_1 &= (0 \quad 1 \quad 0 \quad 1 \quad 0)^{\mathrm{T}} \\ \boldsymbol{\xi}_1 &= (1 \quad 0 \quad 1)^{\mathrm{T}} \\ \boldsymbol{\eta}_2 &= (1 \quad 0 \quad 1 \quad 0 \quad 1)^{\mathrm{T}} \\ \boldsymbol{\xi}_2 &= (0 \quad 1 \quad 0)^{\mathrm{T}} \end{aligned}. \tag{5}$$

Note that, by letting $W_x = W_y = 0$ and by expanding the subsequent expression, one obtains the seven-element hexagonal AF reported by Motes *et al.* [6]. Substituting the expression for a_{mn} into Eq. (4) and subsequent simplification produces

$$\begin{aligned} \mathrm{AF} &= \left(\sum_{m=-2}^{2}\eta_{1m}e^{j2\pi W_y m}e^{jk\hat{\mathbf{r}}\cdot\hat{\mathbf{y}}\frac{D}{2}m}\right)\left(\sum_{n=-1}^{1}\xi_{1n}e^{j2\pi W_x n}e^{jk\hat{\mathbf{r}}\cdot\hat{\mathbf{x}}\frac{D\sqrt{3}}{2}n}\right) \\ &\quad + \left(\sum_{m=-2}^{2}\eta_{2m}e^{j2\pi W_y m}e^{jk\hat{\mathbf{r}}\cdot\hat{\mathbf{y}}\frac{D}{2}m}\right)\left(\sum_{n=-1}^{1}\xi_{2n}e^{j2\pi W_x n}e^{jk\hat{\mathbf{r}}\cdot\hat{\mathbf{x}}\frac{D\sqrt{3}}{2}n}\right) \\ &= \mathrm{AF}_y^{2\times2}\mathrm{AF}_x^{2\times2} + \mathrm{AF}_y^{3\times1}\mathrm{AF}_x^{3\times1}. \end{aligned} \tag{6}$$

Expressing the AF in this form yields much physical insight. The first line product of Eq. (6) corresponds to the y and x AFs of the 2×2 rectangular array produced by elements 2, 4, 5, and 7, respectively. For brevity, these terms are hereafter represented as $\mathrm{AF}_y^{2\times2}$ and $\mathrm{AF}_x^{2\times2}$. The second line product corresponds to the y and x AFs of the 3×1 linear array produced by elements 1, 3, and 6, respectively. Hereafter, these terms are represented as $\mathrm{AF}_y^{3\times1}$ and $\mathrm{AF}_x^{3\times1}$. Since this contribution to the total AF is that of a linear array oriented in y, $\mathrm{AF}_x^{3\times1} = 1$. Note that Eq. (6) repeats when

$$\begin{aligned} W_x &= W_x' + \frac{p+q}{2} \\ W_y &= W_y' + \frac{p-q}{2}, \end{aligned} \tag{7}$$

where p and q are integers. Stated simply, identical radiated fields are produced when the changes in the x and y array tilts are integer multiples of 1/2 whose sum equals an integer.

Before progressing to the derivation of the radiated power, it is worth noting that analyzing hexagonal arrays in the fashion just presented is novel and very powerful. The AFs of all arrays with elements arranged in a regular hexagon decompose in the manner outlined above. For instance, the AFs for the 19- and 37-element hexagonal arrays are

$$\begin{aligned} \mathrm{AF}_{19} &= \mathrm{AF}_y^{5\times1}\mathrm{AF}_x^{5\times1} + \mathrm{AF}_y^{4\times2}\mathrm{AF}_x^{4\times2} + \mathrm{AF}_y^{3\times2}\mathrm{AF}_x^{3\times2} \\ \mathrm{AF}_{37} &= \mathrm{AF}_y^{7\times1}\mathrm{AF}_x^{7\times1} + \mathrm{AF}_y^{6\times2}\mathrm{AF}_x^{6\times2} + \mathrm{AF}_y^{5\times2}\mathrm{AF}_x^{5\times2} \\ &\quad + \mathrm{AF}_y^{4\times2}\mathrm{AF}_x^{4\times2}, \end{aligned} \tag{8}$$

where $\mathrm{AF}_x^{5\times1} = \mathrm{AF}_x^{7\times1} = 1$.

B. Far-Field Radiated Power

Since the radiated power is primarily used to estimate array tilt, its derivation is included here. The far-field radiated power is given by

$$\begin{aligned} I^{\mathrm{rad}}(\boldsymbol{r}) &\propto \boldsymbol{E}^{\mathrm{rad}}(\boldsymbol{r})\cdot\boldsymbol{E}^{\mathrm{rad}*}(\boldsymbol{r}) \\ &\propto \frac{k^2}{r^2}\left[\left(\frac{d}{2}\right)^2\frac{J_1(k\frac{d}{2}\sin\theta)}{k\frac{d}{2}\sin\theta}\right]^2 \\ &\quad \times (\boldsymbol{e}^{\mathrm{rad}}\cdot\boldsymbol{e}^{\mathrm{rad}*})\mathrm{AF}(\theta,\phi)\mathrm{AF}^*(\theta,\phi) \\ &\propto I^{\mathrm{el}}(\theta)|\mathrm{AF}(\theta,\phi)|^2, \end{aligned} \tag{9}$$

where $*$ denotes a complex conjugate. Substituting Eq. (6) into Eq. (9) and subsequent simplification yields

$$\begin{aligned} I^{\mathrm{rad}}(\boldsymbol{r}) &\propto I^{\mathrm{el}}(\theta)|\mathrm{AF}_x^{2\times2}|^2|\mathrm{AF}_y^{2\times2}|^2 + I^{\mathrm{el}}(\theta)|\mathrm{AF}_y^{3\times1}|^2 \\ &\quad + I^{\mathrm{el}}(\theta)2\,\mathrm{Re}(\mathrm{AF}_x^{2\times2}\mathrm{AF}_y^{2\times2}\mathrm{AF}_y^{3\times1*}). \end{aligned} \tag{10}$$

The first term in Eq. (10) is the far-field power contribution due to the 2×2 rectangular array composed of elements 2, 4, 5, and 7. For convenience, this term is hereafter referred to as $I^{2\times2}$. The second term is the power contribution due to the 3×1 linear array, comprising elements 1, 3, and 6—hereafter referred to as $I^{3\times1}$. The third term "couples" the 2×2 and 3×1 arrays together, and is hereafter represented as I^c. As will be shown, I^c drives the behavior of the far-field radiated power and, thus, is the most important term when it comes to estimating the amount of array tilt present.

Duplicate radiated power patterns are produced when Eq. (7) is satisfied—exactly the same as the far-zone radiated field. This is somewhat counterintuitive. Because power is proportional to the magnitude squared of the field, one would expect duplicate power patterns to occur at twice the frequency of duplicate field patterns. Note that this is precisely the case for traditional rectangular arrays. The fact that this does not occur for the seven-element hexagonal array has important implications for estimating array tilt and is entirely due to I^c.

For N greater than seven-element regular hexagonal arrays, the basic form of Eq. (10) holds; however, the number of "coupling" power terms increases.

For instance, the far-field radiated power for the 19-element hexagonal array is

$$
\begin{aligned}
I_{19}^{\mathrm{rad}}(\boldsymbol{r}) \propto\ & I^{\mathrm{el}}(\theta)|\mathrm{AF}x4\times 2|^2|\mathrm{AF}_y^{4\times 2}|^2 \\
& + I^{\mathrm{el}}(\theta)|\mathrm{AF}_x^{3\times 2}|^2|\mathrm{AF}_y^{3\times 2}|^2 + I^{\mathrm{el}}(\theta)|\mathrm{AF}_y^{5\times 1}|^2 \\
& + I^{\mathrm{el}}(\theta)2\,\mathrm{Re}(\mathrm{AF}_x^{4\times 2}\mathrm{AF}_y^{4\times 2}\mathrm{AF}_y^{5\times 1*}) \\
& + I^{\mathrm{el}}(\theta)2\,\mathrm{Re}(\mathrm{AF}_x^{3\times 2}\mathrm{AF}_y^{3\times 2}\mathrm{AF}_y^{5\times 1*}) \\
& + I^{\mathrm{el}}(\theta)2\,\mathrm{Re}(\mathrm{AF}_x^{4\times 2}\mathrm{AF}_y^{4\times 2}\mathrm{AF}_x^{3\times 2*}\mathrm{AF}_y^{3\times 2*}), \quad (11)
\end{aligned}
$$

where the "coupling" terms, again, drive the behavior of the far-field radiated power.

C. Correlation-Based Array-Tilt Estimators

Because they are equivalent to the radar-matched filter used to detect targets in signals heavily corrupted by noise [15], correlation-based estimators are typically utilized to estimate array tilt for optical phased arrays [13]. For correlation-based estimators, the x and y array-tilt estimates, $\tilde{W}_x$ and $\tilde{W}_y$, are solutions to

$$
\underset{\tilde{W}_x,\tilde{W}_y\in(-0.5,0.5]}{\mathrm{argmax}} \quad \Gamma(W_x, W_y|\tilde{W}_x, \tilde{W}_y), \quad (12)
$$

where W_x and W_y are the actual amounts of x and y array tilt present. The function Γ is a correlation function given by

$$
\Gamma = \int_{-\infty}^{\infty} I^{\mathrm{rad}}(\boldsymbol{\rho}, L|W_x, W_y) I^{\mathrm{rad}}(\boldsymbol{\rho}, L|\tilde{W}_x, \tilde{W}_y)\mathrm{d}^2\rho. \quad (13)
$$

Note that, in writing Γ, it has been assumed that the paraxial condition holds; thus, L is the distance in z between the source and observation planes and $\boldsymbol{\rho} = \hat{x}x + \hat{y}y$ is the transverse observation vector.

Unfortunately, the form of I^{rad} does not permit analytical evaluation of Γ. Figure 2 shows Γ for $W_x = 0.4$ and $W_y = -0.15$ evaluated numerically. Figure 2(a) shows Γ computed for the seven-element hexagonal array. For comparison, Fig. 2(b) shows Γ computed for the 2×2 rectangular array comprising elements 2, 4, 5, and 7. Note the two maxima in Fig. 2(a) versus the four maxima in Fig. 2(b). The maxima in Fig. 2(a) occur at $(\tilde{W}_x, \tilde{W}_y) = (0.4, -0.15)$ and $(-0.1, 0.35)$ consistent with the duplicate power pattern conditions given in Eq. (7). The four maxima in Fig. 2(b) occur at $(\tilde{W}_x, \tilde{W}_y) = (0.4, -0.15)$, $(0.4, 0.35)$, $(-0.1, -0.15)$, and $(-0.1, 0.35)$ or at twice the frequency of the hexagonal array.

This difference means little if one builds a test correlation matrix containing every combination of x and y array tilts, i.e., a test matrix containing N^2 far-field power patterns. This is rather inefficient. A better alternative would be to estimate the amounts of x and y array tilt independently, thus, requiring a test matrix containing $2N$ patterns.

Figure 2 shows an example of why estimating the amounts of x and y array tilt independently on the hexagonal array can be problematic. Estimating x and y array tilts independently is equivalent to finding the x and y maxima of Γ along the contours denoted by the white dots in Fig. 2. For the seven-element hexagonal array [Fig. 2(a)], this procedure yields an incorrect array-tilt estimate, shown on the figure as a white ×. For the 2×2 rectangular array [Fig. 2(b)], the resulting estimate initially appears erroneous—again, shown on the figure as a white ×. The matched estimate, however, is a duplicate power pattern to the true pattern; thus, the matched estimate is ultimately correct.

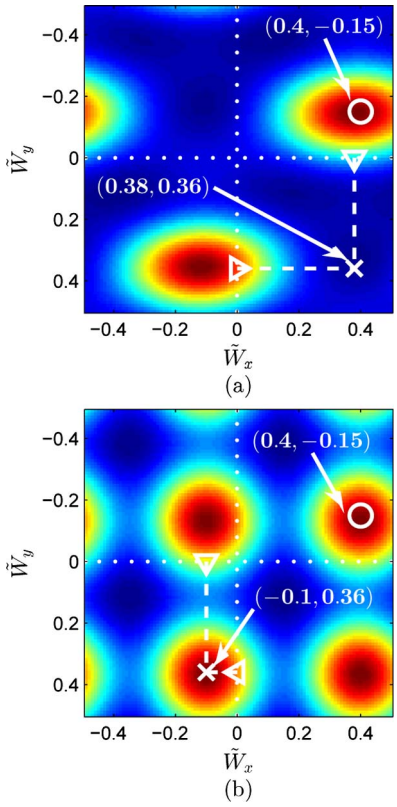

Fig. 2. $\Gamma(0.4, -0.15|\tilde{W}_x, \tilde{W}_y)$ for the (a) seven-element hexagonal and (b) 2×2 rectangular arrays.

Figure 3 yields more insight into the above result. The figure shows the true, $W_x = 0.4$ and $W_y = -0.15$ (in the first row), and matched, $\tilde{W}_x = 0.38$ and $\tilde{W}_y = 0.36$ (in the second row), $I^{2\times 2}$, $I^{3\times 1}$, I^c, and I^{rad} with $D = 1.1d$. The roles played by $I^{2\times 2}$, $I^{3\times 1}$, and I^c in forming I^{rad} are evident in the figure—recall that $I^{\mathrm{rad}} = I^{2\times 2} + I^{3\times 1} + I^c$. The basic underlying structure of I^{rad} is due to $I^{2\times 2}$, with $I^{3\times 1}$ slightly elongating the $I^{2\times 2}$ pattern in x. The defining characteristics of I^{rad}, e.g., the locations of bright and dim spots within I^{rad}, are due to I^c, which serves to raise or lower maxima in $I^{2\times 2}$. Thus, I^c is the most important power contribution term when it comes to estimating array tilt.

This last point is clearly evident in Fig. 3. Note that the true and matched $I^{2\times 2}$ and $I^{3\times 1}$ are identical. This is because the erroneous $\tilde{W}_x = 0.38$ and

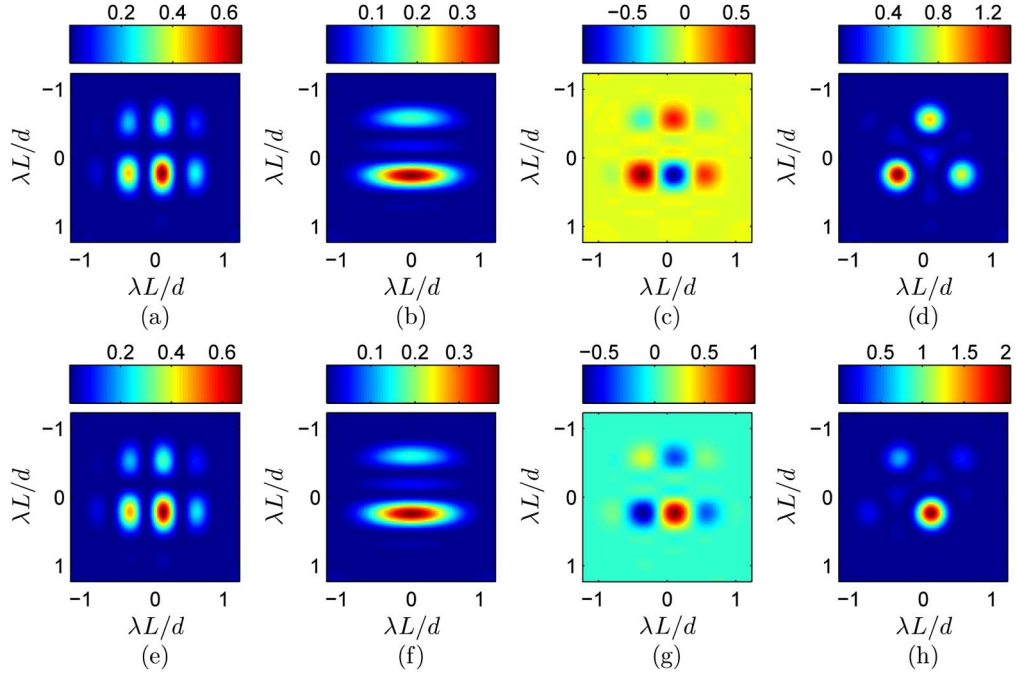

Fig. 3. True ($W_x = 0.4$ and $W_y = -0.15$) and matched ($\tilde{W}_x = 0.38$ and $\tilde{W}_y = 0.36$) $I^{2\times2}$—(a) and (e), respectively; $I^{3\times1}$—(b) and (f), respectively; I^c—(c) and (g), respectively; and I^{rad}—(d) and (h), respectively. The element spacing $D = 1.1d$.

$\tilde{W}_y = 0.36$ are correct (a duplicate pattern to the true pattern) for the rectangular array contributions to I^{rad}. The incorrect array-tilt estimate is ultimately due to I^c, with the true and matched I^c differing only in sign.

It should be noted that, although the preceding discussion focused on the case of $W_x = 0.4$ and $W_y = -0.15$, this case is representative of all instances in which an erroneous $\tilde{W}_x$ and $\tilde{W}_y$ are obtained by estimating x and y array tilts independently. While it is not mathematically accurate to state that the sign of I^c cannot be determined when the x and y array tilts are estimated independently using a correlation-based estimator, this is ultimately the effect.

In the next two sections, two methods are presented that allow x and y array tilts to be estimated independently and still yield accurate results. The two methods make use of the insights gained from the preceding analysis.

1. *Method 1 (Parallel Method)*

As shown in Fig. 3, when estimating x and y array tilts independently on the seven-element hexagonal array, the sign of I^c (effectively) cannot be determined. Thus, it makes sense to estimate the x and y array tilts independently and then test for the sign of I^c.

This process is shown as a flowchart in Fig. 4. The method takes as inputs the "measured" far-field radiated power pattern I^{meas} and two test matrices each containing N I^{rad}—N for x array tilts and N for y array tilts. The x and y array tilt values are then estimated in parallel, as was done in the previous section. From these estimates ($\tilde{W}_x$ and $\tilde{W}_y$), $I^{2\times2}$, $I^{3\times1}$, and I^c are computed. The rectangular array power terms, $I^{2\times2}$ and $I^{3\times1}$, are then summed and subsequently subtracted from I^{meas} to yield the "measured coupling" term $I^{\text{meas},c}$. This term and I^c are then correlated to determine the correct sign of I^c. If the sign of the correlation is negative, then the

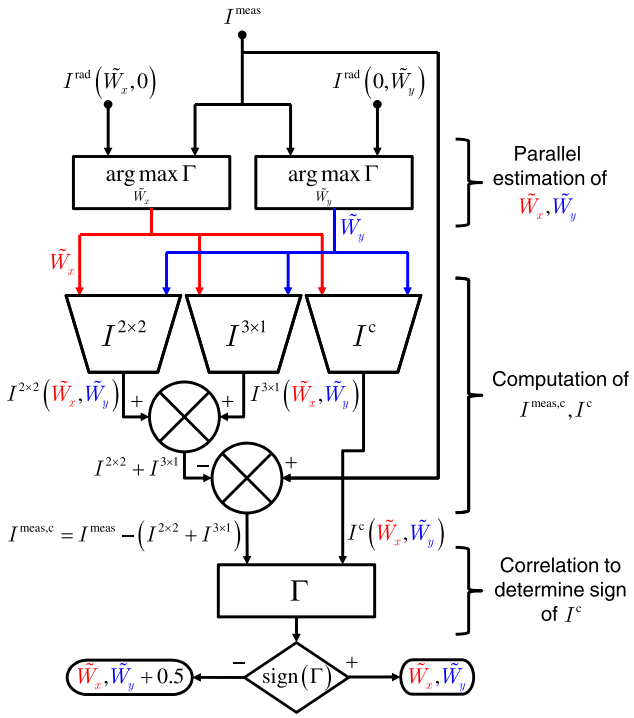

Fig. 4. Parallel method for estimating x and y array tilts.

correct estimates are $\tilde{W}_x$ and $\tilde{W}_y + 0.5$. Note that 0.5 could be added or subtracted to either $\tilde{W}_x$ or $\tilde{W}_y$ and the result will still be correct. If the sign of the correlation is positive, then the initial x and y array-tilt estimates are correct.

Compared with the traditional estimation approach, which requires N^2 correlations, this parallel method requires only $2N + 1$—a significant decrease in computational burden. Although not as significant as the increase in computational efficiency, this new method for estimating x and y array tilts also requires less computer memory than the traditional approach.

2. *Method 2 (Serial Method)*

The second method presented here derives from the observation that an incorrect array-tilt estimate occurs when $\tilde{W}_x$ equals the true x value and $\tilde{W}_y$ equals the duplicate pattern y value, or vice versa. Note that this is precisely what occurred for the $W_x = 0.4$ and $W_y = -0.15$ case discussed above (see Fig. 2). Thus, an accurate array-tilt estimate can be obtained by estimating the x and y array tilts serially.

This process is shown as a flowchart in Fig. 5. The method takes as inputs I^{meas} and a test matrix containing N x array-tilt I^{rad}. The x array tilt is then estimated. From this estimate ($\tilde{W}_x$), a test matrix containing N y array-tilt I^{rad} is then computed. The resulting I^{rad} test matrix is then correlated with I^{meas} to determine $\tilde{W}_y$. Note that starting with I^{meas} and a test matrix containing N y array-tilt I^{rad} would also yield the correct result.

Like the first method, there are significant savings in terms of computation and memory using the serial method versus the traditional approach. The serial method requires one less correlation computation compared with the parallel approach ($2N$ versus $2N + 1$); however, this advantage comes at the cost of having to compute the correlations serially.

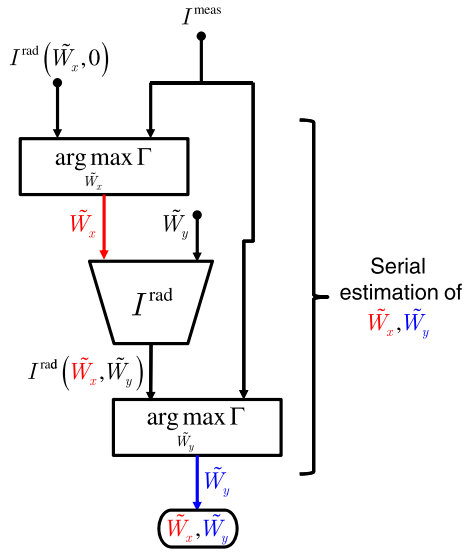

Fig. 5. Serial method for estimating x and y array tilts.

3. Validation

This section presents simulation and experimental results implementing the methods discussed above. Brief descriptions of the simulation and experimental setups are included.

A. Monte Carlo Simulations

Monte Carlo simulations were performed to validate the two array-tilt estimation methods discussed in the previous section. For these simulations, $\lambda = 632.8$ nm, $L = 5$ m, $d = 0.95$ mm, and $D = 1.1d = 1.045$ mm. The "measured" radiated power I^{meas} was formed from randomly chosen W_x and W_y, between -0.5 and 0.5 waves. The correlation test matrices were formed from I^{rad} calculated from x and y array-tilt values between -0.48 and 0.5, in steps of 0.02 waves. The I^{meas} and the images comprising the correlation test matrices were 100 pixel × 100 pixel images and physically measured 8.12 mm × 8.12 mm, or $2.44\lambda L/d \times 2.44\lambda L/d$. The mean and standard deviation of the error ($\bar{e}$ and σ_e, respectively), i.e.,

$$e = |W_x - \tilde{W}_x| + |W_y - \tilde{W}_y|, \tag{14}$$

were computed over 5000 trials for the traditional, parallel (method 1), and serial (method 2) estimation approaches. Array-tilt estimates, which yielded duplicate far-field power patterns, were considered correct in the error calculation. To show how the various estimation methods performed in the presence of noise, $\bar{e}$ and σ_e were computed for differing levels of photon noise.

Figure 6 and Table 1 report the results. The level of noise is reported as mean counts $\bar{K}$ and is the average number of photons per pixel in I^{meas}. An example simulation trial result is shown in Fig. 7. Overall, all three methods are highly accurate and relatively

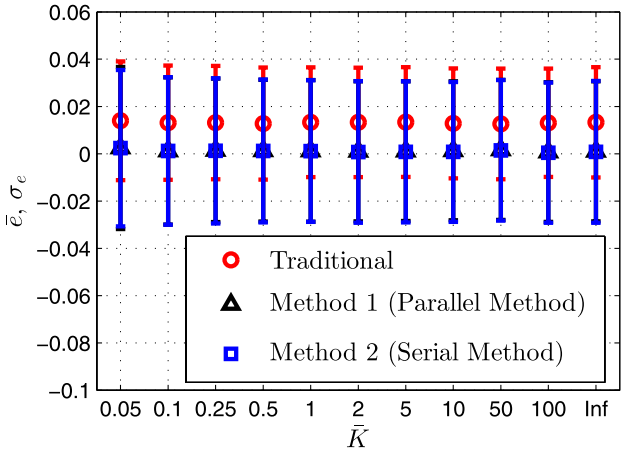

Fig. 6. Mean and standard deviation of the error versus mean counts $\bar{K}$.

Table 1. Simulation Array-Tilt Estimation Results

	Traditional		Method 1 (Parallel Method)		Method 2 (Serial Method)	
$\bar{K}$	$\bar{e}$	σ_e	$\bar{e}$	σ_e	$\bar{e}$	σ_e
0.05	0.0139	0.0251	0.0024	0.0343	0.0024	0.0331
0.1	0.0131	0.0242	0.0012	0.0311	0.0012	0.0312
0.25	0.0132	0.0240	0.0014	0.0303	0.0012	0.0307
0.5	0.0127	0.0237	0.0013	0.0300	0.0012	0.0302
1	0.0133	0.0232	0.0012	0.0300	0.0011	0.0300
2	0.0133	0.0232	0.0010	0.0296	0.0008	0.0300
5	0.0134	0.0232	0.0011	0.0296	0.0008	0.0299
10	0.0129	0.0232	0.0013	0.0294	0.0008	0.0296
50	0.0126	0.0234	0.0016	0.0296	0.0014	0.0297
100	0.0131	0.0229	0.0007	0.0295	0.0005	0.0297
∞	0.0133	0.0234	0.0010	0.0296	0.0008	0.0300

insensitive to noise. Note that there is no statistical difference in performance between the three array-tilt estimation approaches; thus, the new algorithms introduced in Section 2 are (on average) just as accurate as the traditional method.

B. Experiment

A schematic of the experimental setup is shown in Fig. 8. Light leaves a 30 mW 632.8 nm He–Ne laser and enters a 15× beam expander. Upon exiting the beam expander, the light passes through a half-wave plate (HWP) and a linear polarizer (LP). These two polarization elements serve two purposes: the first is to align the linear polarization state of the light exiting the laser to the control linear polarization state of the spatial light modulator (SLM). This is accomplished using the LP. The second is to coarsely control the power incident on the SLM. This is accomplished using the HWP.

After passing through the HWP and LP, the light is incident on the SLM. The SLM in the experiment is a 512 × 512 Boulder Nonlinear Systems, Inc. Model P512-0635 SLM [16]. The seven-element hexagonal array pattern, as well as an artificial diffraction grating and the desired amount of array tilt, are commanded onto the SLM face. The sawtooth-shaped diffraction grating serves to maximize the power in the first diffraction order, which is in the direction

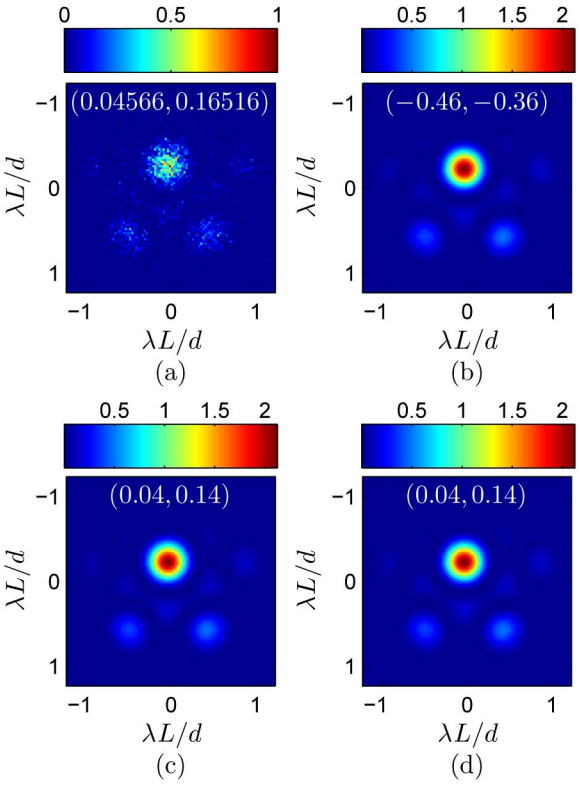

Fig. 7. Example simulation trial for $\bar{K} = 0.25$—(a) I^{meas}, (b) I^{rad} traditional, (c) I^{rad} method 1, and (d) I^{rad} method 2. The true value of array tilt is annotated on (a); the estimated values are annotated on (b), (c), and (d).

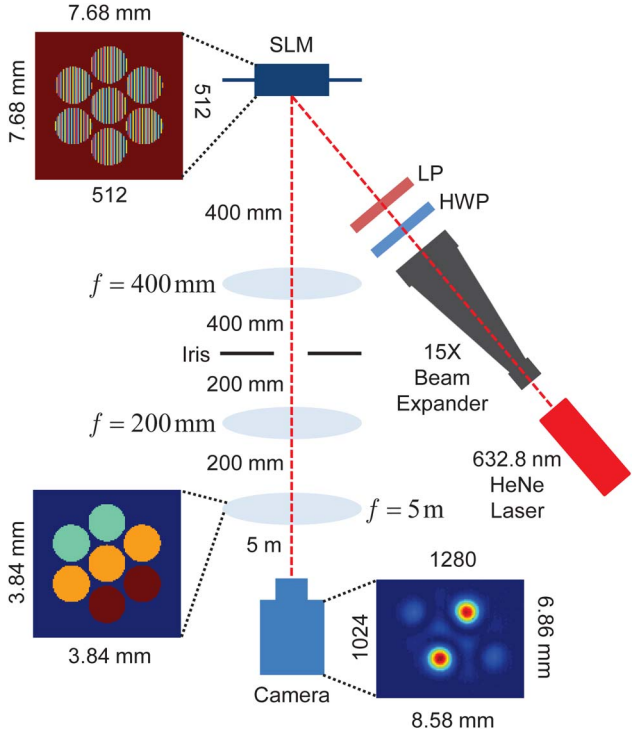

Fig. 8. Schematic of the experimental setup.

of the camera. An example SLM command image is shown in Fig. 8. The diameter d of the circular array elements in the command image is 1.9 mm. The element spacing $D = 1.1d = 2.09$ mm. Note that only the SLM pixels comprising the seven-element hexagonal array are commanded. Light scattered from the uncommanded pixels is "carried off" in the zeroth diffraction order.

After reflecting from the SLM, the desired light in the first diffraction order propagates along the detector leg of the apparatus. The detector leg consists of three lenses, a 400 mm, 200 mm, and 5 m, all positioned at focus; an iris; and a Lumenera Corp. Lu125M camera [17]. The lens system, composed of the 400 and 200 mm lenses, serves to image the SLM face at half-size at the 5 m lens location. An example image of the SLM face at the 5 m lens location is shown in Fig. 8. A $W_x = 0.25$ and $W_y = 0.25$ example pattern is shown in the image. Note that, in reality, one would not be able to visualize the relative phasing between array elements; the image is only illustrative. The iris placed at the Fourier plane of the 400 mm lens is used to remove diffraction orders other than the desired first order, which are inadvertently collected by the 400 mm lens. Lastly, the 5 m lens serves to Fourier-transform the half-size image of the SLM face. This yields the desired far-field seven-element hexagonal array power pattern, which is subsequently recorded by the camera. An example $W_x = 0.25$ and $W_y = 0.25$ camera image is shown in Fig. 8.

As was the case for the simulation results discussed above, the correlation test matrices were formed from I^{rad} calculated from x and y array-tilt values between −0.48 and 0.5, in steps of 0.02 waves. The 1280×1024 I^{meas} were decimated to 128×128 (6.75 mm × 6.75 mm) to match the size of the images in the correlation test matrices. The mean and standard deviation of the error were computed over 2500 trials for the traditional, parallel (method 1), and serial (method 2) estimation approaches. The number of trials was reduced because of experimental runtime (approximately 3 h to perform 2500 trials). Array-tilt estimates, which yielded duplicate far-field power patterns, were considered correct in the experimental error calculation.

The results are presented in Table 2. Figure 9 shows an example experimental trial result. In agreement with the simulation results discussed above, there is no statistical difference in performance between the three array-tilt estimation techniques. Thus, it can be concluded that the overall performance of the parallel and serial methods is comparable with the traditional approach.

Table 2. Experimental Array-Tilt Estimation Results

	$\bar{e}$	σ_e
Traditional	0.0050	0.0294
Method 1 (Parallel method)	0.0150	0.0232
Method 2 (Serial method)	0.0142	0.0264

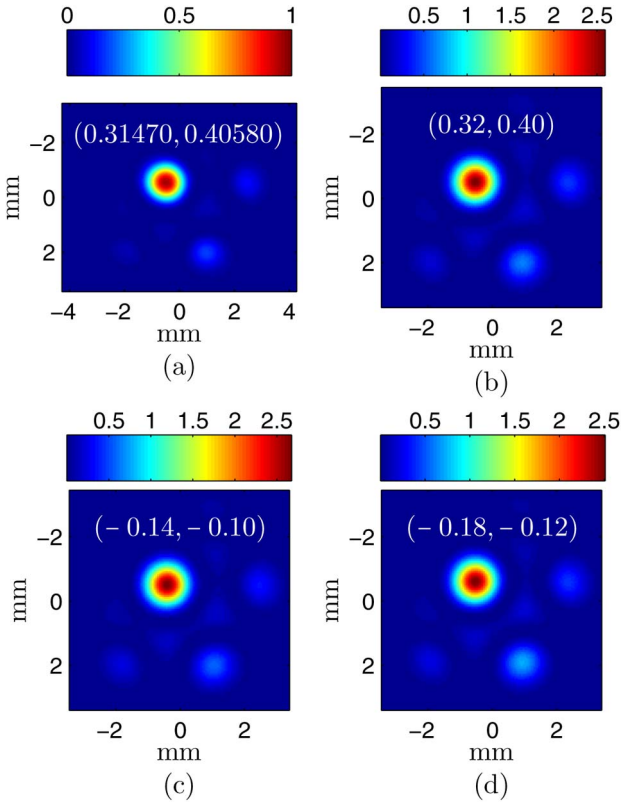

Fig. 9. Example experimental trial—(a) I^{meas}, (b) I^{rad} traditional, (c) I^{rad} method 1, and (d) I^{rad} method 2. The true value of array tilt is annotated on (a); the estimated values are annotated on (b), (c), and (d).

4. Conclusions

In this paper, a rigorous analytical investigation of the array-tilt aberration for hexagonal, optical phased arrays was performed. Theoretical expressions for the far-zone radiated electric field, the AF, and the far-field radiated power for the seven-element hexagonal array were derived and discussed. Significant physical insight into the behavior of the array was gained through analysis of these analytical forms. An analytical treatment of correlation-based array-tilt estimators was also undertaken. Two novel array-tilt estimation methods (the parallel and serial methods) were presented. The new techniques were shown to be significantly more efficient computationally than the traditional estimation approach. Lastly, simulations and experiments were performed to verify the new estimation algorithms. It was found that the new methods were comparable in performance with the traditional technique. These empirical results, when combined with the increase in computational efficiency, make the parallel and serial methods viable alternatives to the traditional array-tilt estimation approach.

It should be noted that while the purpose of this paper was to present and test correlation-based

alternatives to the traditional method for estimating array tilt, much remains to be explored for the practical use of correlation-based array-tilt estimators in general. For example, the effects of atmospheric turbulence, platform jitter (manifested as uncentered I^{meas}), target-induced speckle, and imager entrance pupil size on the quality of the array-tilt estimate still require research.

The views expressed in this paper are those of the authors and do not reflect the official policy or position of the U.S. Air Force, the Department of Defense, or the U.S. Government.

References

1. S. E. Lamberson, "The airborne laser," Proc. SPIE **4760**, 25–33 (2002).
2. D. T. Kyrazis, "Airborne laser laboratory departure from Kirtland Air Force Base and a brief history of aero-optics," Opt. Eng. **52**, 071403 (2013).
3. G. Forden, "The airborne laser," IEEE Spectrum **34**, 40–49 (1997).
4. B. Wang, E. Mies, M. Minden, and A. Sanchez, "All-fiber 50 W coherently combined passive laser array," Opt. Lett. **34**, 863–865 (2009).
5. T. Fan, "Laser beam combining for high-power, high-radiance sources," IEEE J. Sel. Top. Quantum Electron. **11**, 567–577 (2005).
6. R. A. Motes, S. A. Shakir, and R. W. Berdine, *Introduction to High Power Fiber Lasers*, 2nd ed. (Directed Energy Professional Society, 2013).
7. P. Bourdon, V. Jolivet, B. Bennai, L. Lombard, G. Canat, E. Pourtal, Y. Jaouen, and O. Vasseur, "Coherent beam combining of fiber amplifier arrays and application to laser beam propagation through turbulent atmosphere," Proc. SPIE **6873**, 687316 (2008).
8. R. J. Pawlak, "Recent developments and near term directions for Navy Laser Weapons System (LaWS) testbed," Proc. SPIE **8547**, 854705 (2012).
9. P. Bondyopadhyay, "The first application of array antenna," in *IEEE International Conference on Phased Array Systems and Technology* (IEEE, 2000), pp. 29–32.
10. A. Flores, T. Shay, C. Lu, C. Robin, B. Pulford, A. Sanchez, D. Hult, and K. Rowland, "Coherent beam combining of fiber amplifiers in a kW regime," in *Conference on Lasers and Electro-Optics* (Optical Society of America, 2011), paper CFE3.
11. T. M. Shay, "Theory of electronically phased coherent beam combination without a reference beam," Opt. Express **14**, 12188–12195 (2006).
12. G. A. Tyler, "Accommodation of speckle in object-based phasing," J. Opt. Soc. Am. A **29**, 722–733 (2012).
13. M. F. Spencer and M. W. Hyde, "An investigation of stair mode in optical phased arrays using tiled apertures," Proc. SPIE **8520**, 852006 (2012).
14. C. A. Balanis, *Antenna Theory: Analysis and Design*, 3rd ed. (Wiley, 2005).
15. M. I. Skolnik, *Introduction to Radar Systems*, 3rd ed. (McGraw-Hill, 2001).
16. Boulder Nonlinear Systems, Inc., Spatial Light Modulators—XY Series (Retrieved November 16, 2013.
17. Lumenera Corporation, Lu120, Lu125 1.3 Megapixel USB 2.0 Camera (Retrieved November 16, 2013 from http://www.lumenera.com/resources/documents/datasheets/industrial/Lu120-Lu125-datasheet.pdf).